



Steering charge transfer for boosting photocatalytic H₂ evolution: Integration of two-dimensional semiconductor superiorities and noble-metal-free Schottky junction effect

Xiaojie She^a, Hui Xu^{a,*}, Li Li^a, Zhao Mo^a, Xingwang Zhu^a, Yahui Yu^a, Yanhua Song^b, Jingjie Wu^c, Junchao Qian^d, Shouqi Yuan^a, Huaming Li^a

^a Institute for Energy Research, School of the Environment and Safety Engineering, Jiangsu University, Zhenjiang 212013, PR China

^b School of Environmental and Chemical Engineering, Jiangsu University of Science and Technology, Zhenjiang 212003, PR China

^c Department of Chemical and Environmental Engineering, University of Cincinnati, Cincinnati, OH 45221, USA

^d School of Chemistry, Biology and Materials Engineering, Suzhou University of Science and Technology, Suzhou, 215009, PR China

ARTICLE INFO

Keywords:

2D materials

Schottky junction

Photocatalytic H₂ evolution

ABSTRACT

Sunlight-driven photocatalysis holds great promise for alleviating the energy and environmental crises. For the visible-light-driven bare semiconductor, there is an irreconcilable contradiction between the light absorption and strong redox capabilities. Here, we reported a predictable design for improving the photocatalytic performance via regulating the bandgap and accelerating the charge kinetics of the semiconductor. Taken together, utilize two-dimensional (2D) structure to essentially increase the bandgap of the semiconductor for gaining the higher transfer and separation of the photogenerated electron-hole pairs and the stronger redox capabilities; and accelerate charge kinetics via the driving force from the Schottky junction. Meanwhile, the Schottky barrier prevents the photogenerated electrons trapped by a noble-metal-free electron acceptor from dually recombining. Additionally, the energy transfer process of the photocatalytic reaction was also researched in detail, aligning well with the photocatalytic mechanism.

1. Introduction

Photocatalysis as the most promising technology for addressing energy and environmental crises is widely used in water spitting, CO₂ reduction as well as wastewater treatment [1–8]. The photocatalytic reaction is a redox reaction participated in by the photogenerated electrons and holes from the semiconducting photocatalyst. The conduction band (CB) and valence band (VB) of the semiconductor determine the redox capability and the rate of the photocatalytic redox reaction depends on the charge kinetics of the semiconductor [8–10]. Within certain limits, the CB and VB of the semiconductor should be higher (more negative) and lower (more positive), respectively, meaning a wide bandgap (E_g) semiconductor possesses the strong redox capability [10–12]. As the wide band-gap semiconductor can only absorb the short-wavelength UV light, however, there is an irreconcilable contradiction between the visible light absorption and strong redox capabilities because UV light with short-wavelength only takes ~4% and the visible light with long wavelength takes ~46% of the incoming solar energy. For another, the photogenerated charge carriers from the

bare semiconductor can only diffuse irregularly due to the lack of the charge driving force, resulting in the slow charge kinetics [9,10]. To rationally design the photocatalyst, the above factors need to be considered.

For the band structure of the semiconductor, it should be increased as high as possible without limiting the absorption of the visible light, that is the absorption edge should be larger than 400 nm ($\lambda > 400$ nm, $E_g < 3.1$ eV). Generally, decreasing the size of the bare semiconductor is an effective method for increasing the bandgap. Especially, when the size is reduced to the nano level, the semiconductor will possess the quantum confinement effect, which can effectively increase the bandgap of the semiconductor [13–16]. As there are so many indeterminacies for simultaneously decreasing three-dimensional (3D) sizes of the semiconductor for the photocatalytic reaction, however, 2D semiconductors with a nano-size in the Z direction have attracted lots of attentions [17,18]. 2D semiconducting photocatalysts with an ultrathin structure possess a larger bandgap than that of the bulk one and the higher transfer and separation efficiencies of the charge carriers from the bulk to the surface [19–21]. Thus, controllably adjusting the

* Corresponding author.

E-mail address: xh@ujs.edu.cn (H. Xu).

<https://doi.org/10.1016/j.apcatb.2018.12.011>

Received 13 September 2018; Received in revised form 27 November 2018; Accepted 3 December 2018

Available online 04 December 2018

0926-3373/ © 2018 Elsevier B.V. All rights reserved.

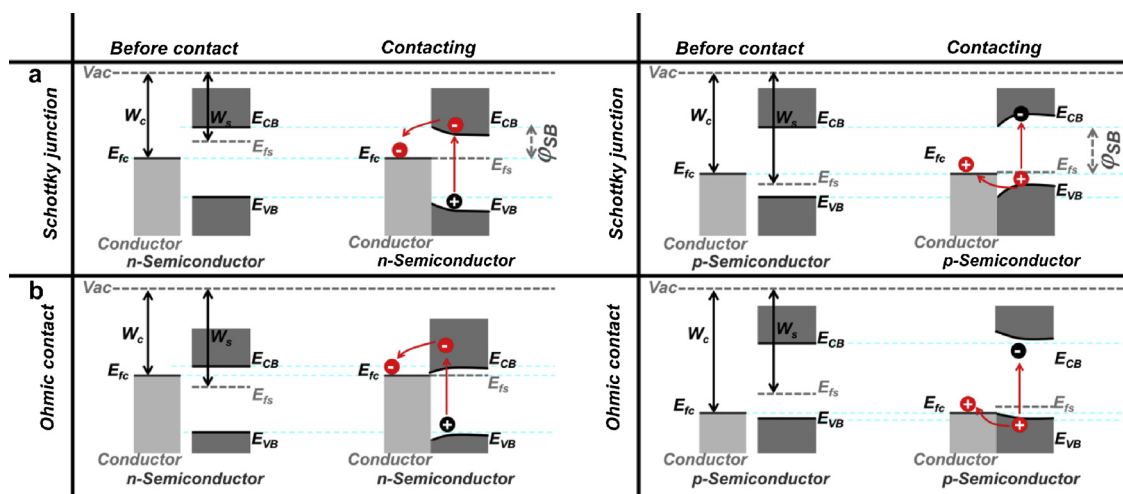


Fig. 1. Design mechanism diagram from the band illustrating for the Schottky junction (a) and the ohmic contact (b) of the n-Type and the p-Type semiconductor with the conductor.

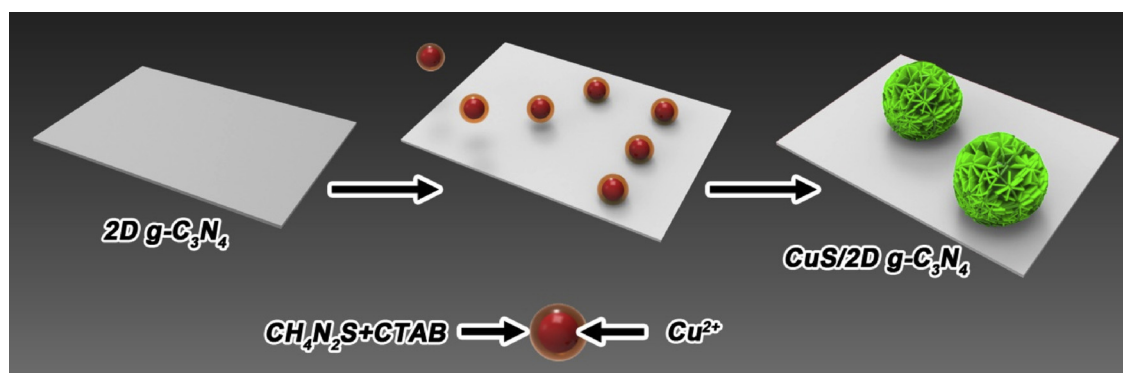


Fig. 2. Schematic illustration of the synthetic process of CuS/2D g-C₃N₄.

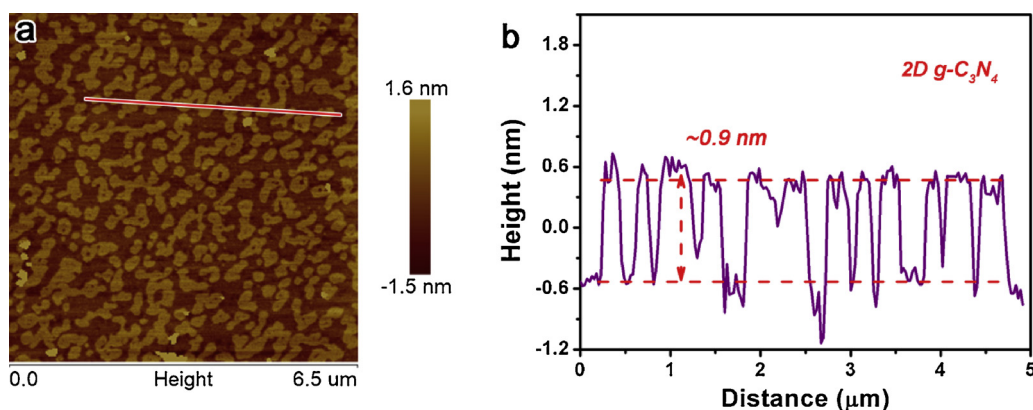


Fig. 3. (a) AFM image of 2D g-C₃N₄, (b) the corresponding height image of the red line for 2D g-C₃N₄. (For interpretation of the references to colour in this figure legend, the reader is referred to the web version of this article).

thicknesses of some semiconductors is a high-efficiency method for increasing the bandgap.

To accelerate charge kinetics of the photocatalytic reaction, integrating the conductors (mainly noble metal such as Pt, Au and Ag) to the semiconductors is a commonly effective method for improving the photocatalytic performance [9,22–26]. There are mainly two combination modes for conductor-semiconductor heterojunction (the Schottky junction and the ohmic contact), as shown in Fig. 1. Take n-Type semiconductor as an example, when the work function of the conductor (W_c) is larger than that of the n-Type semiconductor (W_s)

and then come into contact, to build up an equilibrium state between the Fermi levels of the conductor (E_{fc}) and n-Type semiconductor (E_{fs}), the electrons from the n-Type semiconductor will diffuse to the conductor at a lower energy level, resulting in the upward band bend from semiconductor to conductor and the Schottky barrier (ϕ_{SB}) (Schottky junction) will form (the left side of Fig. 1a) [9,27,28]. Certainly, W_c may be smaller than W_s , the downward band bending will form and no barrier forms, meaning an ohmic contact (the left side of Fig. 1b) [9,29]. For the p-Type semiconductor, the Schottky junction and ohmic contact are shown in the right side of Fig. 1. It is obvious that the charge

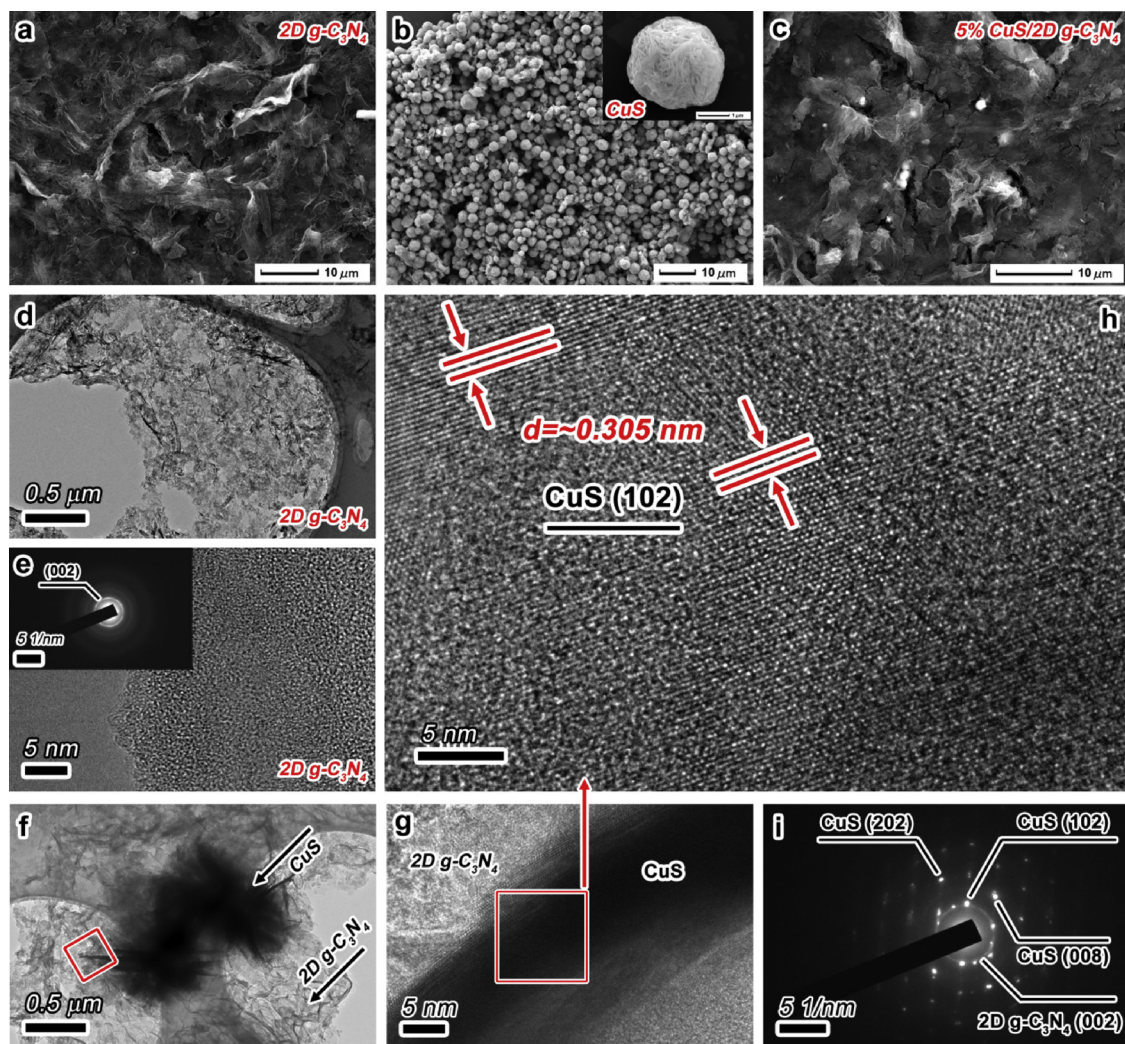


Fig. 4. FE-SEM images of (a) 2D g-C₃N₄, (b) CuS and (c) 5% CuS/2D g-C₃N₄ composite, TEM images of (d) 2D g-C₃N₄ and (f) 5% CuS/2D g-C₃N₄, HR-TEM of (e) 2D g-C₃N₄, (g and h) 5% CuS/2D g-C₃N₄ composite, (the inset of e and i) SAED patterns of 2D g-C₃N₄ and 5% CuS/2D g-C₃N₄ composite.

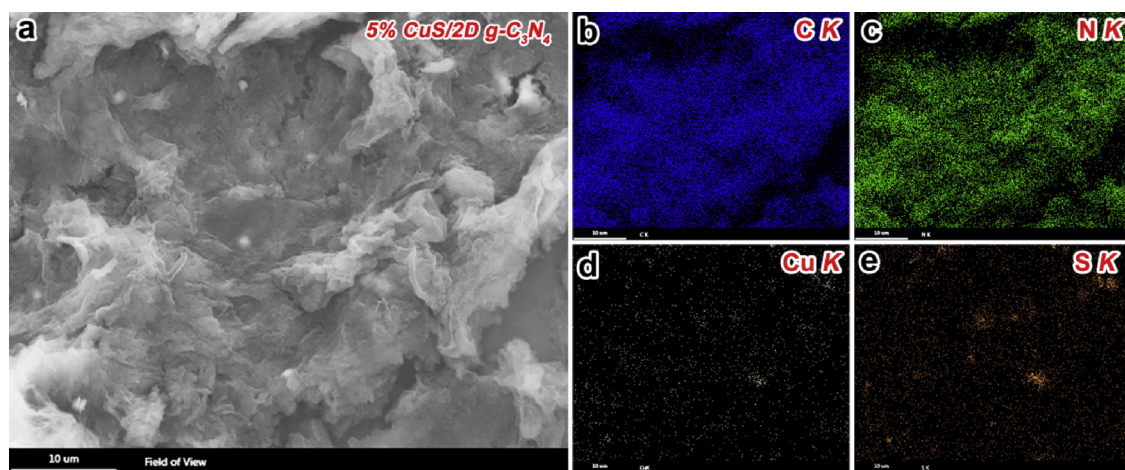


Fig. 5. SEM image of (a) 5% CuS/2D g-C₃N₄ composite, (b–e) EDS elemental mappings from C, N, Cu and S, corresponding to (a).

carriers transfer in ohmic contact should be smoother compared with that of the Schottky junction due to no barrier in ohmic contact [29]. However, the charge carriers can also return to the semiconductor by the ohmic contact due to no barrier, resulting in the recombination of the charge carriers. Generally, the efficiency of the Schottky junction is

higher than that of the ohmic contact for the separation or suppression of the charge carriers [30,31]. Although the noble metals, especially platinum (Pt), possess the absolute advantages in the conductor-semiconductor system due to the large work function, this is not acceptable for the commerce [32–35]. Thus, the noble-metal-free conductors are

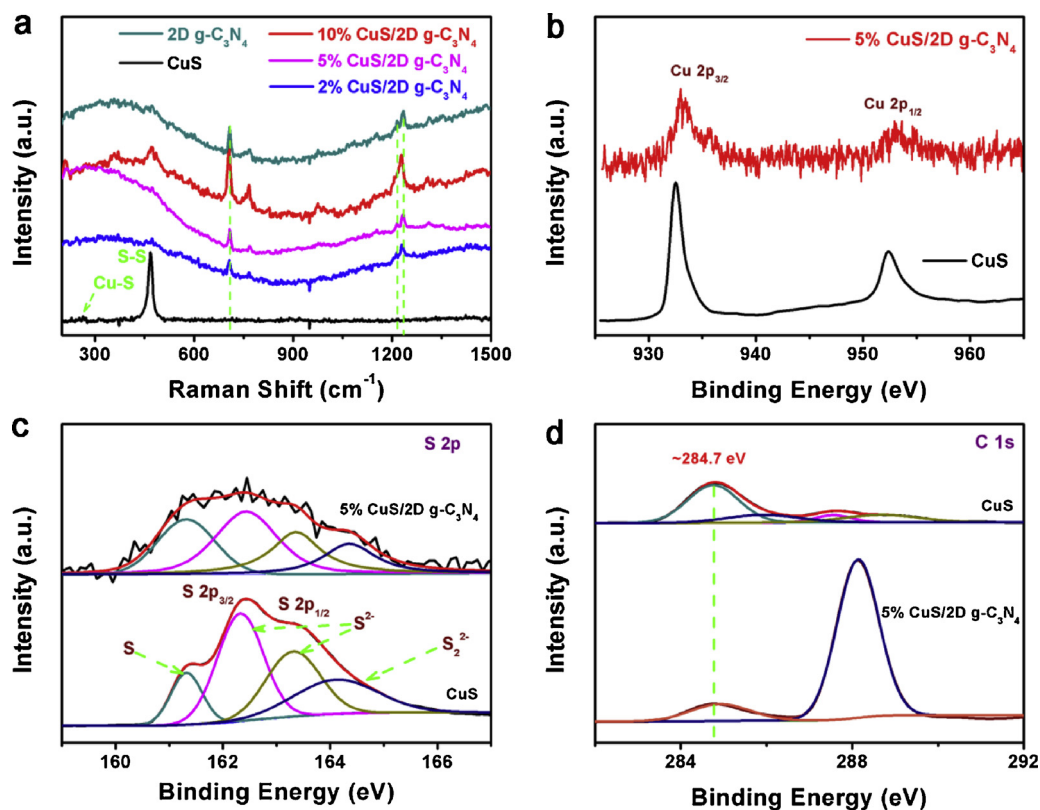


Fig. 6. (a) Raman spectra of the samples, (b–d) the high-resolution XPS spectra of Cu 2p, S 2s and C 1s from the pure CuS and 5% CuS/2D g-C₃N₄ composite.

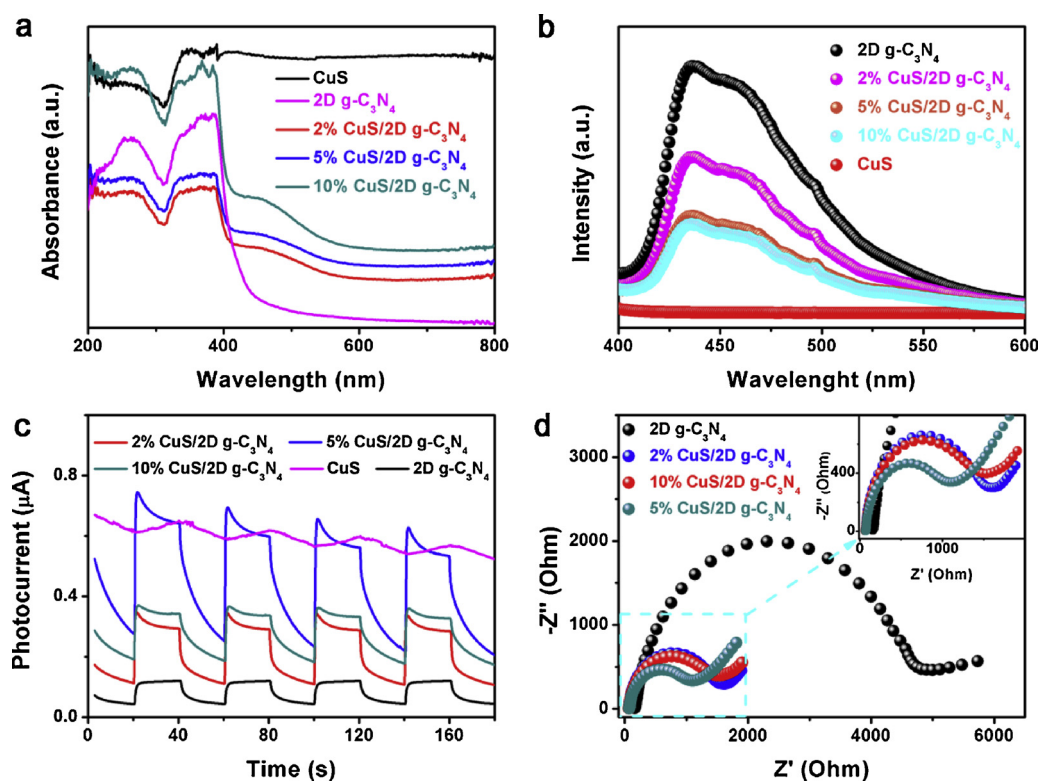


Fig. 7. (a) UV-vis diffuse reflectance spectra, (b) PL spectra excited at 383 nm, (c) Photocurrent-time dependence under visible light irradiation and (d) EIS of the samples.

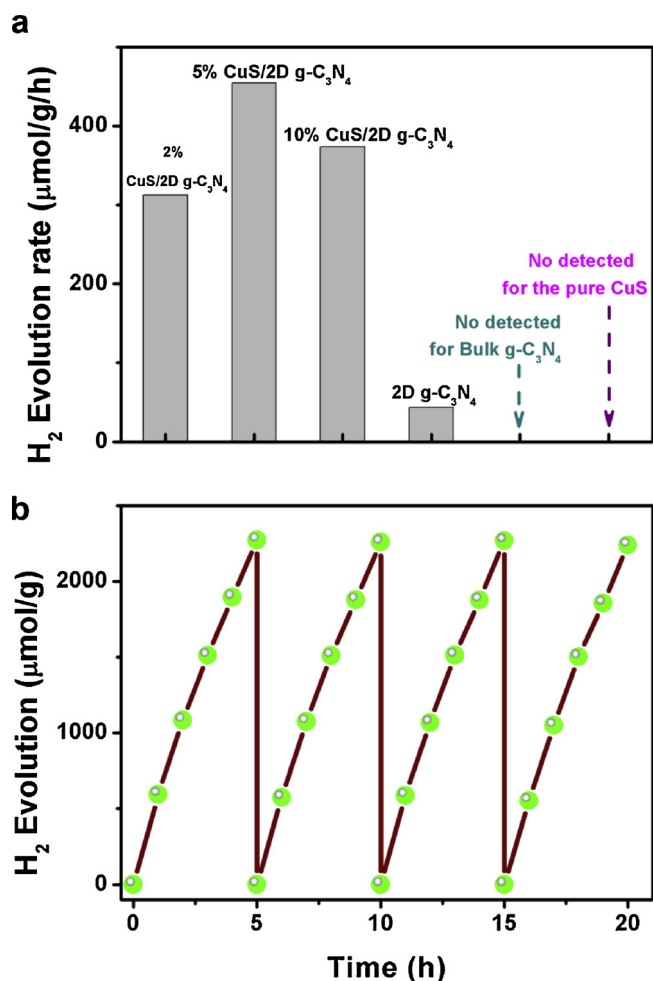


Fig. 8. (a) Photocatalytic H₂ evolutions from the water of the samples under the visible-light irradiation with TEOA as the sacrificial agent, (b) Stability test of 5% CuS/2D g-C₃N₄ for the photocatalytic H₂ evolution.

naturally considered.

In this work, we synergistically utilized 2D semiconductor superiorities and noble-metal-free Schottky junction effect to boost the photocatalytic H₂ evolution performance. As a proof of concept, we chose CuS with a large work function as an electron acceptor to assemble on the surface of the ultrathin 2D g-C₃N₄ with a larger bandgap and the higher transfer and separation efficiencies compared with the bulk g-C₃N₄ via the *in-situ* growth method. Compared with the bulk g-C₃N₄, the photocatalytic H₂ evolution performance of 2D g-C₃N₄ was improved from zero to “one” without any co-catalyst. And the introduction of CuS in 2D g-C₃N₄ further boosted the photocatalytic activity. The process of the charge carriers transfer and the photocatalytic mechanism were researched in detail.

2. Experimental section

2.1. Chemicals

Melamine (C₃H₆N₆, > 99.0%), Copper(II) nitrate trihydrate (Cu(NO₃)₂·3H₂O, > 99.0%), Thiourea (CH₄N₂S, > 99.0%), Ethylene glycol (EG, C₂H₆O₂, ≥ 99.0%), Cetyl trimethyl ammonium bromide (CTAB, C₁₉H₄₂BrN, ≥ 99.0%), Ethanol absolute (C₂H₆O, ≥ 99.7%) and Triethanolamine (TEOA, C₆H₁₅NO₃, AR) were purchased from Sinopharm Chemical Reagent Co., Ltd. (China). All chemicals were used as received without further purification. Deionized water was used through all experiments.

2.2. Synthesis of the samples

2D g-C₃N₄ was prepared by a modified method based on the previous report [36]. Firstly, the bulk g-C₃N₄ was synthesized. 2 g of Melamine was calcined at 550 °C for 4 h and the obtained bulk g-C₃N₄ was ground into powder. Then, the bulk g-C₃N₄ powder was further calcined at 550 °C for ~110 min. The obtained white sample was denoted as 2D g-C₃N₄ due to possessing a two-dimensional nanosheet structure.

CuS/2D g-C₃N₄ was synthesized by an *in-situ* solvothermal method. In a typical synthesis, a certain amount of Cu(NO₃)₂·3H₂O (0.005 g, 0.0126 g and 0.0253 g), 0.1 g of 2D g-C₃N₄ and 0.006 g of Thiourea were dispersed in a mixed solution containing 10 mL EG and 30 mL deionized water. Then, 0.003 g of CTAB was added to the above suspension under magnetic stirring. After stirring for 30 min, the suspension was sonicated for another 30 min. Lastly, the suspension was heated at 100 °C for 18 h in a Teflon-lined stainless steel autoclave with 50 mL capacity. After cooling to room temperature, the sample was collected by centrifuge and washed with water and ethanol several times. Finally, the sample was freeze-dried for 24 h. And the different mass ratios of composites were denoted as 2%, 5% and 10% CuS/2D g-C₃N₄.

The pure CuS was prepared by the above method as that for CuS/2D g-C₃N₄, except the addition of 2D g-C₃N₄.

2.3. Photoelectrochemical measurement

The samples were dispersed in the mixed solution containing ethanol and EG (1:1 by volume) to form 1 mg/mL suspension by sonication. 40 μL of the suspension was drop-casted onto a 0.5 cm × 1 cm² indium tin oxide-coated glass (ITO), and dried under an infrared lamp. The photocurrent and electrochemical impedance spectroscopy (EIS) were tested on a CHI 760E electrochemical station (Shanghai Chenhua, China) in ambient environment under irradiation of a 300 W Xe lamp, in which a standard three-electrode system was used with Pt wire as a counter electrode, the sample/ITO as the working electrode and a Ag/AgCl electrode as the reference electrode. 0.1 M NaSO₄ solution was used as the electrolyte for the photocurrent measure. In the photocurrent experiment, the bias potential was set to 0. Additionally, EIS measures were carried out in the frequency range of 10⁻¹ to 10⁵ Hz. AC voltage amplitude is 5 mV and the bias potential is 0.24 V vs. Ag/AgCl in a 5 mM impedance liquid Fe(CN)₆³⁻/Fe(CN)₆⁴⁻.

2.4. Photocatalytic H₂ production measurements

To investigate the photocatalytic activity of samples for H₂ evolution, TEOA (Triethanolamine) was used to sacrifice the holes. 0.01 g of samples were added to 100 mL TEOA/H₂O (1:9 by volume) and then sonicated to form a uniform suspension, followed by VD vacuum degassing to remove the air. 300 W Xe lamp (PLS-SXE300, PerfectLight, Beijing, China) with a 400 nm long-wave-pass cut-off filter (i.e., λ > 400 nm) was used to irradiate. The amount of H₂ evolved was determined using gas chromatography (GC, D7900T, TCD detector, Ar carrier, 5 Å molecular sieve column).

3. Results and discussion

As only when there is an intimate contact between an electron acceptor and a semiconductor can the Schottky junction be formed [9]. In this case, the *in-situ* growth method was used to synthesize composite photocatalysts with the Schottky junction. In the proof-of-concept demonstration, 2D g-C₃N₄ and CuS were employed as a model 2D photocatalyst and an electron acceptor to boost the photocatalytic H₂ production from H₂O under the visible light integrating 2D semiconductor superiorities and noble-metal-free Schottky junction effect. The synthetic strategy of CuS/2D g-C₃N₄ composites includes two steps.

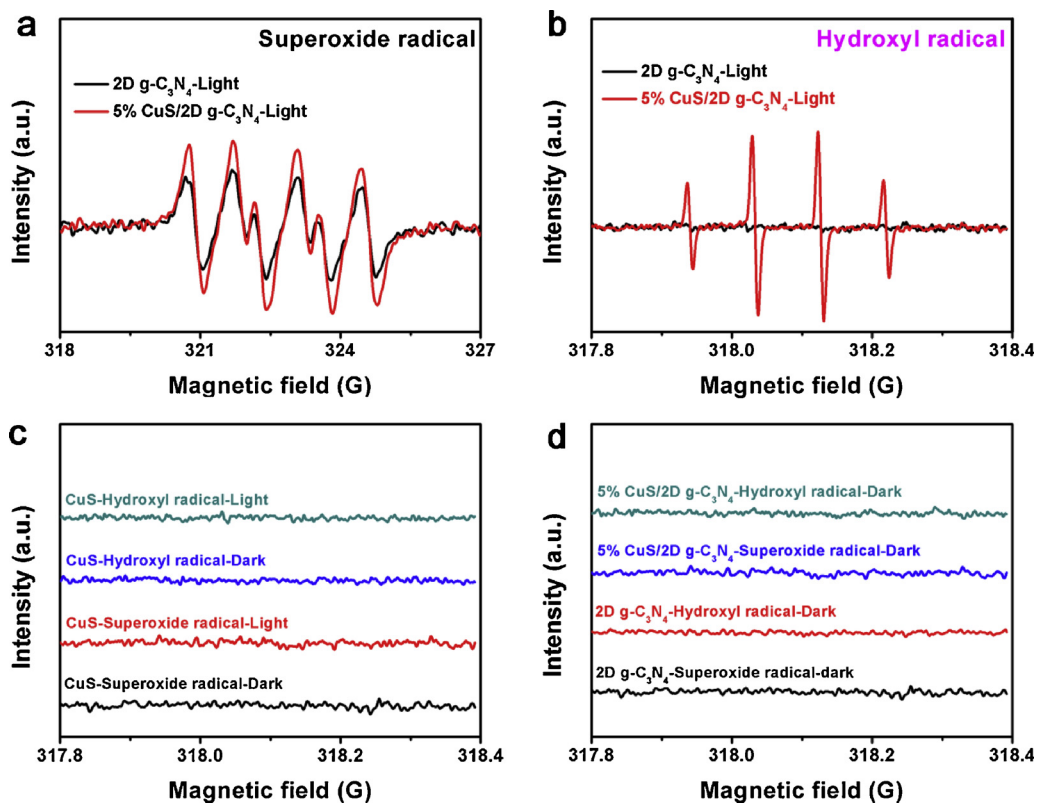


Fig. 9. ESR spectra of (a) DMPO-O₂•⁻ and (b) •OH adducts under the visible-light irradiation of the pure 2D g-C₃N₄ and 5% CuS/2D g-C₃N₄, (c and d) ESR spectra of DMPO-O₂•⁻ and •OH adducts under the dark or light for the pure CuS, 2D g-C₃N₄ and 5% CuS/2D g-C₃N₄.

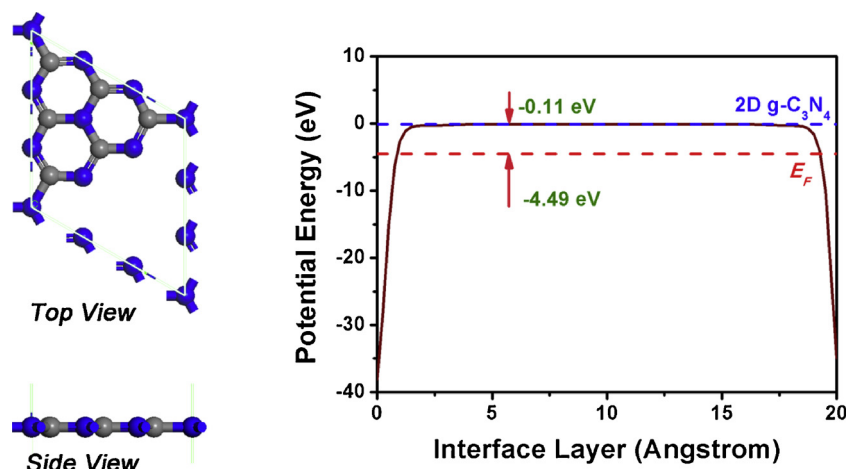


Fig. 10. Simulation models of 2D monolayer g-C₃N₄ (the left side), the potential diagram of 2D monolayer g-C₃N₄ (the right side).

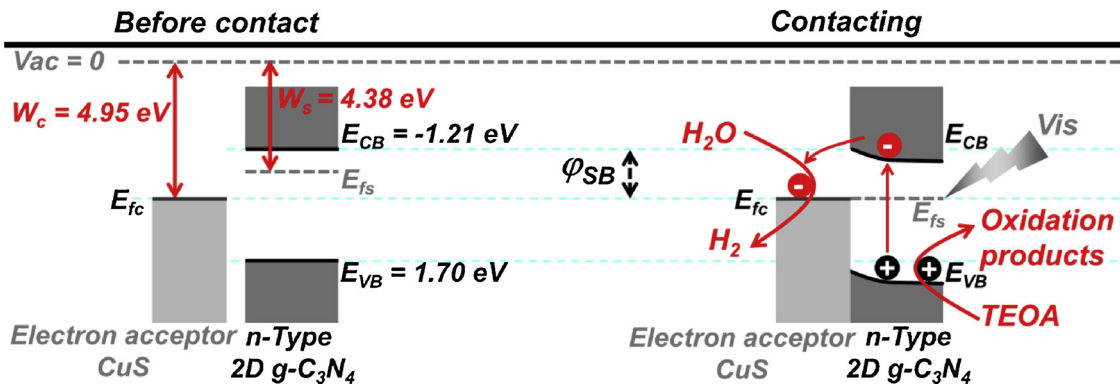


Fig. 11. Schematic photocatalytic mechanism of the CuS/2D g-C₃N₄ composite by the band structure.

Firstly, to obtain 2D semiconducting photocatalyst, 2D g-C₃N₄ was prepared by a multi-step calcination process. The color of the obtained fluffy 2D g-C₃N₄ turns from yellow to white (Fig. S1). Secondly, assemble CuS on the surface of 2D g-C₃N₄ via the *in-situ* solvothermal method, as shown in Fig. 2. In the synthetic process, CTAB was served as a control agent, CH₄N₂S as the S source for CuS.

The crystalline structures of the as-synthesized samples were firstly confirmed (Fig. S2). The X-ray diffraction (XRD) peaks can be well assigned to g-C₃N₄. The peaks at $\sim 27.7^\circ$ are derived from the interlayer stacking reflection (002), and those at $\sim 13.1^\circ$ (the in-plane repeated units of (100)) are obviously expanded and the intensities are decreased in comparison with the previous reports, due to the 2D structure [36,37]. The corresponding XRD peaks of CuS do not emerge in the composites due to the relatively low content of CuS. XRD patterns show that the crystal structure of g-C₃N₄ is not changed in the synthetic process. The Fourier transform infrared (FT-IR) spectra (Fig. S3) shows all samples possess a similar chemical structure, corresponding to that of g-C₃N₄. The bands at $\sim 810\text{ cm}^{-1}$ are derived from the stretching vibration model of the s-triazine units, the bands on the range of ~ 1800 to 900 cm^{-1} are attributed to C=N and C-N vibration and the broad ones from ~ 3600 to 3000 cm^{-1} can be assigned to O-H and N-H vibration [38]. From the above analyses, it can be known the structure of 2D g-C₃N₄ is kept very well.

To resolve the 2D g-C₃N₄ thickness, the atomic force microscope (AFM) was employed to measure the sample (Fig. 3). Fig. 3a shows the obtained 2D g-C₃N₄ emerges the uniform and typical 2D nanosheet structure and the thickness is $\sim 0.9\text{ nm}$ (Fig. 3b). Fig. 4 shows the structures of all samples, characterized by the field emission scanning electron microscope (FE-SEM), transmission electron microscope (TEM) and selected area electron diffraction (SAED). From SEM images (Fig. 4a–c), it can be known that 2D g-C₃N₄ is of the like-silk nanosheet structure, CuS exhibits the uniform flower-like structure consisted of CuS nanosheets, and for the composites, the flower-like CuS is tightly anchored on the surface of 2D g-C₃N₄. Additionally, TEM images of 2D g-C₃N₄ and 5% CuS/2D g-C₃N₄ composite are shown in Fig. 4d–h. 2D g-C₃N₄ is of the nanosheet structure and almost transparent to the electron beam, indicating 2D g-C₃N₄ possesses an ultrathin 2D structure (Fig. 4d). The high-resolution transmission electron microscope (HR-TEM) shows there is no any distinctly ordered lattice fringe on the surface of 2D g-C₃N₄ (Fig. 4e). The diffraction ring from the selected area electron diffraction (SAED) pattern (the inset of Fig. 4e) is indexed to the (002) plane of 2D g-C₃N₄, which corresponds with the XRD result of 2D g-C₃N₄. From Fig. 4f, it can be known that the flower-like CuS was anchored on the surface of 2D g-C₃N₄ via the *in-situ* growth method and 2D structure of 2D g-C₃N₄ was not destroyed in the synthesis process. Fig. 4g and h (HR-TEM images of 5% CuS/2D g-C₃N₄) correspond to regions inside the red line quadrates of Fig. 4f and g, respectively. As indicated by Fig. 4g, the intimate contact is formed between CuS and 2D g-C₃N₄, which is very beneficial to the establishment of the Schottky junction. CuS shows obvious and ordered lattice fringes with the lattice spacing of $\sim 0.305\text{ nm}$, which is ascribed to the (102) crystal plane (JCPDS 06-0464). As presented in SAED image of 5% CuS/2D g-C₃N₄ composite, the diffraction spots of the (102), (202) and (008) planes from CuS and the diffraction ring of the (002) plane from 2D g-C₃N₄ can be clearly observed (Fig. 4i), indicating that CuS in the composite is the hexagonal single-crystal structure with the space group P6₃/mmc [39]. To confirm the components of the samples, the elemental distributions were measured by FE-SEM and energy-dispersive spectroscopy (EDS) mapping (Fig. 5 and S4), revealing that the obtained CuS is only composed of Cu and S, and CuS had been anchored on the surface of 2D g-C₃N₄. Taken together, CuS/2D g-C₃N₄ composites with the intimate contact interface have been prepared successfully.

Fig. 6a shows Raman spectra analysis excited with UV-laser at 532 nm on all samples. For CuS, there are two peaks (a weak one at $\sim 264.3\text{ cm}^{-1}$ and a sharp one at $\sim 470.6\text{ cm}^{-1}$), corresponding to the vibrational modes from Cu–S and S–S bonds, respectively, which

shows CuS is of the single-crystal structure [39–41]. Intuitively, the composites show nearly identical Raman shifts of 2D g-C₃N₄, the crystal structure of 2D g-C₃N₄ is retained after the *in-situ* synthesis. Three peaks located at ~ 708.1 , 1215.1 and 1230.6 cm^{-1} are the characteristic peaks of the graphite carbon nitride [13]. Additionally, with the increase of CuS content in the composites, the peaks of CuS is stronger and stronger. To gain insights into the surface chemical states, X-ray photoelectron spectroscopy (XPS) was employed to characterize CuS and 5% CuS/2D g-C₃N₄, as shown in Figs. 6b–c and S5. For the pure CuS and composite, two strong peaks at ~ 932.1 and 952.2 eV can be observed, assigned to Cu 2p_{3/2} and Cu 2p_{1/2} (Fig. 6b) [41]. And S 2p XPS spectra of the samples can be deconvoluted into four subpeaks at ~ 161.2 , 162.3 , 163.1 and 164.2 eV (Fig. 6c), corresponding to S 2p_{3/2}, S 2p_{1/2}, S₂^{2−} and S^{2−} [38,39,42], respectively. All XPS spectra were calibrated with C 1s (284.7 eV), as shown in Fig. 6d. The high-resolution XPS spectra of C 1s and N 1s of 5% CuS/2D g-C₃N₄ are the typical characters of the g-C₃N₄, as shown in Figs. 6d and S5b.

The optical properties of the samples were tested via UV–vis diffuse reflectance spectroscopy (DRS). As indicated by UV–vis DRS (Fig. 7a), the introduction of CuS increases the absorption intensity in the whole visible light region, which may mean a limited increase in the utilization of solar energy. Additionally, it can be found the absorption edges of the composites did not obviously shift compared with that of the pure 2D g-C₃N₄, indicating that the introduction of CuS did not change the band gap of 2D g-C₃N₄ which is $\sim 2.91\text{ eV}$ (Fig. S6). Fig. 7b shows the photoluminescence (PL) spectra of the samples. In principle, the intensity of PL can reflect the separation and recombination of the semiconducting photogenerated charges, as the recombination induces luminescence. In this case, it's obvious that 2D g-C₃N₄ possessed an evident charge recombination due to the strongest PL intensity. The introduction of CuS results in a significant quicker quenching of PL in comparison with that of 2D g-C₃N₄, meaning the photogenerated electron-hole recombination of CuS/2D g-C₃N₄ composites can be effectively suppressed by the Schottky junction between CuS and 2D g-C₃N₄.

To reveal the photogenerated electron transfer process via the Schottky junction from the semiconductor to the electron acceptor CuS, the photocurrent and electrochemical impedance spectroscopy (EIS) of the samples were characterized (Fig. 7c and d). The high-efficiency Schottky junction effect means the photogenerated electrons from an n-type semiconductor (2D g-C₃N₄) can be effectively trapped by CuS as the electron acceptor. The reflection in the photoelectrochemical system is that the photocurrent of the photocatalyst with the high-efficiency Schottky junction effect can be increased and its EIS decrease. 5% CuS/2D g-C₃N₄ possesses the strongest photoelectric response (Fig. 7c), meaning CuS as the electron acceptor in 5% CuS/2D g-C₃N₄ can most efficiently trap the photogenerated electrons from 2D g-C₃N₄ via the Schottky junction, that is to say, its separating efficiency of the photogenerated electron-hole pairs is the highest. Additionally, the pure CuS with the weak photocurrent response mainly plays a role in trapping the photogenerated electrons from 2D g-C₃N₄ via the Schottky junction. And the high basic current of the pure CuS shows it's an excellent electron acceptor. EIS Nyquist plot (Fig. 7d) also reveals 5% CuS/2D g-C₃N₄ has the smallest radius, corresponding to PL and the photocurrent of the samples. The above results demonstrate the Schottky junction between CuS and 2D g-C₃N₄ has been established successfully.

Upon acquiring the function of 2D structure superiorities and Schottky junction effect, we are in a position to better carry out g-C₃N₄-based composites in photocatalysis using the photocatalytic Hydrogen evolution from water as a model reaction without the noble metal co-catalyst. The H₂ evolution reaction is an absolute electron-consuming reduction reaction, which can actually reflect the action of electrons. As demonstrated in Fig. 8a, the bare 2D g-C₃N₄ shows a low photocatalytic activity under the visible light irradiation obviously because the photogenerated electron-hole pairs can't separate effectively. However, the

bulk g-C₃N₄ is inert for H₂ evolution, corresponding to almost all of the previous reports [20,21,36], which shows that the 2D structure of 2D g-C₃N₄ conclusively contributes to boosting photocatalytic H₂ evolution performance. In sharp comparison with the bare 2D g-C₃N₄, the photocatalytic activities of CuS/2D g-C₃N₄ composites rapidly increase. The pure CuS is also inert for the photocatalytic H₂ evolution. The above results identify the function of the 2D structure and Schottky junction in the photocatalysis. Additionally, 5% CuS/2D g-C₃N₄ exhibits the highest H₂ evolution activity which is of the reason that a large amount of CuS would prevent the semiconductor from absorbing the light and go against the formation of Schottky junction. Thus, there is an optimum content of CuS as the electron acceptor in the composites. After 4 cycles, H₂ evolution rate still maintains for 5% CuS/2D g-C₃N₄ (Fig. 8b). The detailed H₂ evolution dates are shown in Fig. S8.

Upon gathering the above information, we hope to depict the reaction process of H₂ evolution for CuS/2D g-C₃N₄, so as to gain insights into the mechanism of the photocatalytic H₂ evolution. Firstly, the electron spin resonance (ESR) was employed to evaluate the separation efficiency of the photogenerated charge carriers (Fig. 9). As expected, for the pure 2D g-C₃N₄, the ESR signals from O₂^{•−} trapped by 5,5-dimethyl-1-pyrroline N-oxide (DMPO) were observed and there is no any signals from [•]OH due to the limitation of the band-gap structure of the pure 2D g-C₃N₄ (Fig. 9a and b) [20,43]. On the basis of the previous result from Ultraviolet photoelectron spectroscopy (UPS) measurement, it can be known the valence band and conduction band of the pure 2D g-C₃N₄ are 1.70 and −1.21 eV, respectively [36]. No doubt the holes at VB of 2D g-C₃N₄ have no ability to oxidize H₂O/OH[−] into [•]OH, but the electrons at CB can combine with O₂ to form O₂^{•−}. As we irradiated the suspension of DMPO and 5% CuS/2D g-C₃N₄, however, not only the singles of O₂^{•−} but also [•]OH is observed. This is because a mass of the photogenerated electrons captured by CuS via the Schottky junction gather on the surface of the conducting CuS, these captured electrons combine with O₂ to form the excessive O₂^{•−}, whereafter, the excessive O₂^{•−} can combine with the electrons and H⁺ in water to produce [•]OH (O₂ + e[−] → O₂^{•−}, O₂^{•−} + e[−] + 2H⁺ → H₂O₂, H₂O₂ + e[−] → [•]OH + OH[−]) [44–47]. From Fig. 9a and b, the intensities of O₂^{•−} and [•]OH singles from 5% CuS/2D g-C₃N₄ composite are stronger than that of the pure 2D g-C₃N₄, revealing CuS can trap the photogenerated electrons by the Schottky junction and prevent these electrons from flowing back to CB of 2D g-C₃N₄ via the ϕ_{SB} . Thus, the separation efficiency of the photogenerated electron-hole pairs is increased greatly. Additionally, in the dark, ESR has no any signal (Fig. 9b and c). Lastly, to correlate the band structures, the work function (W_s) of the pure 2D g-C₃N₄ was calculated (Fig. 10). The vacuum level (Vac) and Fermi level (E_F) are −0.11 and −4.49 eV, respectively, thus, W_s is 4.38 eV. The work function (W_s) of the pure CuS is 4.95 eV [48]. When CuS is introduced into 2D g-C₃N₄, to set up an equilibrium state between the E_F s and E_{fc} (E_{fc} is Fermi level of CuS), the electrons of 2D g-C₃N₄ flow to CuS at the lower energy level. As a result, a space charge region is formed on the side of 2D g-C₃N₄, which makes energy band bend upward, going from 2D g-C₃N₄ to CuS, thus the ϕ_{SB} is formed, as shown in Fig. 11. Note that the electron flow of CuS is very difficult to change the E_{fc} of its own on account of the high density of the free electrons in CuS. Instead, only the band level of 2D g-C₃N₄ is reduced due to the dense holes left in 2D g-C₃N₄. And according to the results from DRS, it can be known that the absorption edges of 2D g-C₃N₄ in the composites did not change, indicating that the photoinduced interfacial charge transfer (IFCT) can't be tenable [49,50]. Additionally, the electrons trapped by CuS can't flow back to CB of 2D g-C₃N₄ due to the existence of the ϕ_{SB} . The electrons gathered on CuS surface can reduce H₂O to H₂ and the holes on the surface of 2D g-C₃N₄ can oxidize TEOA to the oxidation products, implementing the photocatalytic H₂ evolution from water under the visible light irradiation.

4. Conclusions

In this work, we have taken advantages of 2D semiconductor superpriorities and Noble-Metal-free Schottky junction effect for boosting the photocatalytic performance. 2D g-C₃N₄ can provide a wide-band structure (a stronger redox capability) and a high efficiency of transfer and separation of the photogenerated electron-hole pairs. When CuS comes into 2D g-C₃N₄, the photogenerated electrons can be trapped by CuS via the formed Schottky junction which also can prevent these electrons trapped by CuS from flowing back to CB of 2D g-C₃N₄ via the ϕ_{SB} , which can greatly improve the separation efficiency of the photogenerated electron-hole pairs. As a result, the photocatalytic H₂ evolution performance has been dramatically improved under the visible light irradiation. Additionally, the energy transfer process of the photocatalytic reaction was also researched in detail, aligning well with the photocatalytic mechanism. Although the CuS as the electron acceptor here may be not the case of having the best 3D size, it's a rational design for enhancing photocatalytic performance. This work can provide a consideration in the composite photocatalysts design toward regulating the bandgap and accelerating the charge kinetics.

Acknowledgments

The authors genuinely appreciate the financial support of this work by the National Natural Science Foundation of China (21776118, 21476097). A Project Funded by Natural Science Foundation of Jiangsu Province (BK20180870). A Project Funded by China Postdoctoral Science Foundation (2017M620193) and the Priority Academic Program Development of Jiangsu Higher Education Institutions, High-tech Research Key laboratory of Zhenjiang (SS2018002). The calculation in this work was supported by the high performance computing platform of Jiangsu University.

Appendix A. Supplementary data

Supplementary material related to this article can be found, in the online version, at doi:<https://doi.org/10.1016/j.apcatb.2018.12.011>.

References

- [1] Q. Wang, T. Hisatomi, Q.X. Jia, H. Tokudome, M. Zhong, C.Z. Wang, Z.H. Pan, T. Takata, M. Nakabayashi, N. Shibata, Y.B. Li, I.D. Sharp, A. Kudo, T. Yamada, K. Domen, Nat. Mater. 15 (2016) 611–615.
- [2] Q. Wang, T. Hisatomi, Y. Suzuki, Z. Pan, J. Seo, M. Katayama, T. Minegishi, H. Nishiyama, T. Takata, K. Seki, A. Kudo, T. Yamada, K. Domen, J. Am. Chem. Soc. 139 (2017) 1675–1683.
- [3] R. Long, Y. Li, Y. Liu, S.G. Chen, X.S. Zheng, C. Gao, C.H. He, N.S. Chen, Z.M. Qi, L. Song, J. Jiang, J.F. Zhu, Y.J. Xiong, J. Am. Chem. Soc. 139 (2017) 4486–4492.
- [4] S.C. Lian, M.S. Kodaimati, E.A. Weiss, ACS Nano 12 (2018) 568–575.
- [5] C.Y. Dong, C. Lian, S.C. Hu, Z.S. Deng, J.Q. Gong, M.D. Li, H.L. Liu, M.Y. Xing, J.L. Zhang, Nat. Commun. 9 (2018) 1252.
- [6] J.Y. Li, Z.Y. Zhang, W. Cui, H. Wang, W.L. Cen, G. Johnson, G.M. Jiang, S. Zhang, F. Dong, ACS Catal. 8 (2018) 8376–8385.
- [7] M.Y. Xing, W.J. Xu, C.C. Dong, Y.C. Bai, J.B. Zeng, Y. Zhou, J.L. Zhang, Y.D. Yin, Chemistry 4 (2018) 1359–1372.
- [8] S.W. Cao, B.J. Shen, T. Tong, J.W. Fu, J.G. Yu, Adv. Funct. Mater. 28 (2018) 1800136.
- [9] S. Bai, J. Jiang, Q. Zhang, Y.J. Xiong, Chem. Soc. Rev. 44 (2015) 2893–2939.
- [10] S. Bai, X.Y. Li, Q. Kong, R. Long, C.M. Wang, J. Jiang, Y.J. Xiong, Adv. Mater. 27 (2015) 3444–3452.
- [11] X.J. She, J.J. Wu, H. Xu, Z. Mo, J.B. Lian, Y.H. Song, L. Liu, D.L. Du, H.M. Li, Appl. Catal. B 202 (2017) 112–117.
- [12] Y. Ma, X.L. Wang, Y.S. Jia, X.B. Chen, H.X. Han, C. Li, Chem. Rev. 114 (2014) 9987–10043.
- [13] X.J. She, J.J. Wu, J. Zhong, H. Xu, Y.C. Yang, R. Vajtai, J. Lou, Y. Liu, D.L. Du, H.M. Li, P.M. Ajayan, Nano Energy 27 (2016) 138–146.
- [14] N. Zhang, C. Han, Y.J. Xu, J.J. Foley IV, D.T. Zhang, J. Codrington, S.K. Gray, Y.G. Sun, Nat. Photonics 10 (2016) 473–482.
- [15] X.D. Zhang, H.X. Wang, H. Wang, Q. Zhang, J.F. Xie, Y.P. Tian, J. Wang, Y. Xie, Adv. Mater. 26 (2014) 4438–4443.
- [16] S.J. Xu, D. Li, P.Y. Wu, Adv. Mater. 25 (2014) 1127–1136.
- [17] W.J. Wang, J.C. Yu, Z.R. Shen, D.K.L. Chan, T. Gu, Chem. Commun. 50 (2014) 10148–10150.

- [18] Y. Wang, Y. Liu, J.F. Zhang, J.J. Wu, H. Xu, X.W. Wen, X. Zhang, C.S. Tiwary, W. Yang, R. Vajtai, Y. Zhang, N. Chopra, I.N. Odeh, Y.C. Wu, P.M. Ajayan, *Sci. Adv.* 3 (2017) e1701500.
- [19] X.J. She, H. Xu, Y.G. Xu, J. Yan, J.X. Xia, L. Xu, Y.H. Song, Y. Jiang, Q. Zhang, H.M. Li, *J. Mater. Chem. A* 2 (2014) 2563–2570.
- [20] X.J. She, L. Liu, H.Y. Ji, Z. Mo, Y.P. Li, L.Y. Huang, D.L. Du, H. Xu, H.M. Li, *Appl. Catal. B* 187 (2016) 144–153.
- [21] X.D. Zhang, X. Xie, H. Wang, J.J. Zhang, B.C. Pan, Y. Xie, *J. Am. Chem. Soc.* 135 (2013) 18–21.
- [22] Y.R. Li, Z.W. Wang, T. Xia, H.X. Ju, K. Zhang, R. Long, Q. Xu, C.M. Wang, L. Song, J.F. Zhu, J. Jiang, Y.J. Xiong, *Adv. Mater.* 28 (2016) 6959–6965.
- [23] W.Y. Jiang, S. Bai, L.M. Wang, X.J. Wang, L. Yang, Y.R. Li, D. Liu, X.N. Wang, Z.Q. Li, J. Jiang, Y.J. Xiong, *Small* 12 (2016) 1640–1648.
- [24] S.W. Cao, H. Li, T. Tong, H.C. Chen, A.C. Yu, J.G. Yu, H.M. Chen, *Adv. Funct. Mater.* 28 (2018) 1802169.
- [25] S.W. Cao, Y. Li, B.C. Zhu, M. Jaroniec, J.G. Yu, *J. Catal.* 349 (2017) 208–217.
- [26] S.W. Cao, J. Jiang, B.C. Zhu, J.G. Yu, *Phys. Chem. Chem. Phys.* 18 (2016) 19457–19463.
- [27] A.L. Linsebigler, G.Q. Lu, J.T. Yates, *Chem. Rev.* 95 (1995) 735–758.
- [28] V. Subramanian, E.E. Wolf, P.V. Kamat, *J. Am. Chem. Soc.* 126 (2004) 4943–4950.
- [29] F.P. Yan, Y.H. Wang, J.Y. Zhang, Z. Lin, J.S. Zheng, F. Huang, *ChemSusChem* 7 (2014) 101–104.
- [30] P. Zhou, J.G. Yu, M. Jaroniec, *Adv. Mater.* 26 (2014) 4920–4935.
- [31] D.W. Ding, K. Liu, S.G. He, C.B. Gao, Y.D. Yin, *Nano Lett.* 14 (2014) 6731–6736.
- [32] H. Xu, J.J. Yi, X.J. She, Q. Liu, L. Song, S.M. Chen, Y.C. Yang, Y.H. Song, R. Vajtai, J. Lou, H.M. Li, S.Q. Yuan, J.J. Wu, P.M. Ajayan, *Appl. Catal. B* 220 (2018) 379–385.
- [33] J.M. Cai, Y.M. Zhu, D.S. Liu, M. Meng, Z.P. Hu, Z. Jiang, *ACS Catal.* 5 (2015) 1708–1716.
- [34] B. Han, Y.H. Hu, *Energy Sci. Eng.* 4 (2016) 285–304.
- [35] M. Acerce, D. Voiry, M. Chhowalla, *Nat. Nanotechnol.* 10 (2015) 313–318.
- [36] X.J. She, J.J. Wu, H. Xu, J. Zhong, Y. Wang, Y.H. Song, K.Q. Nie, Y. Liu, Y.C. Yang, M.T.F. Rodrigues, R. Vajtai, J. Lou, D.L. Du, H.M. Li, P.M. Ajayan, *Adv. Energy Mater.* 7 (2017) 1700025.
- [37] C.C. Han, Y. Lu, J.L. Zhang, L. Ge, Y.J. Li, C.F. Chen, Y.J. Xin, L.N. Wu, S.M. Fang, *J. Mater. Chem. A* 3 (2015) 23274–23282.
- [38] X.J. She, H. Xu, H.F. Wang, J.X. Xia, Y.H. Song, J. Yan, Y.G. Xu, Q. Zhang, D.L. Du, H.M. Li, *Dalton Trans.* 44 (2015) 7021–7031.
- [39] S.H. Chaki, J.P. Tailor, M.P. Deshpande, *Mater. Sci. Semicond. Process.* 27 (2014) 577–585.
- [40] A.G. Milekhin, N.A. Yeryukov, L.L. Sveshnikova, T.A. Duda, E.E. Rodyakina, *Beilstein J. Nanotechnol.* 6 (2015) 749–754.
- [41] Y.H. Xiao, D.C. Su, X.Z. Wang, S.D. Wu, L.M. Zhou, Y. Shi, S.M. Fang, H.M. Cheng, F. Li, *Adv. Energy Mater.* 8 (2018) 1800930.
- [42] H.W. Lei, G.J. Fang, F. Cheng, W.J. Ke, P.L. Qin, Z.C. Song, Q. Zheng, X. Fan, H.H. Huang, X.Z. Zhao, *Solar Energy Mater. Solar Cells* 128 (2014) 77–84.
- [43] F. Dong, Z.Y. Wang, Y.H. Li, W.K. Ho, S.C. Lee, *Environ. Sci. Technol.* 48 (2014) 10345–10353.
- [44] M.R. Hoffmann, S.T. Martin, W. Choi, D.W. Bahnemann, *Chem. Rev.* 95 (1995) 69–96.
- [45] Y.J. Cui, J.H. Huang, X.Z. Fu, X.C. Wang, *Catal. Sci. Technol.* 2 (2012) 1396–1402.
- [46] S.C. Yan, Z.S. Li, Z.G. Zou, *Langmuir* 26 (2010) 3894–3901.
- [47] Z.Y. Wang, W. Guan, Y.J. Sun, F. Dong, Y. Zhou, W.K. Ho, *Nanoscale* 7 (2015) 2471–2479.
- [48] M. Basu, R. Nazir, P. Fageria, S. Pande, *Sci. Rep.* 6 (2016) 34738.
- [49] T.J. Chen, C.J. Song, M.S. Fan, Y.Z. Hong, B. Hu, L.B. Yu, W.D. Shi, *Int. J. Hydrogen Energy* 42 (2017) 12210–12219.
- [50] J. Zhang, J.G. Yu, Y.M. Zhang, Q. Li, J.R. Gong, *Nano Lett.* 11 (2011) 4774–4779.